ACIN

Calibration and flight test of a 3D printed 5-hole probe for high-dynamic wind measurements for UAV

Andras Galffy[1], Florian Car, Georg Schitter

Abstract—**This paper focuses on the integration and characterization of a 3D printed 5-hole probe for high-dynamic wind measurements for UAV. The probe is calibrated by means of a free jet wind tunnel and validated by dynamic angle of attack variations during an unmanned test flight. The angle of attack and sideslip angle measurements show an RMS error of $24\,\mathrm{mrad}$ with a peak-to-peak noise of $3\,\mathrm{mrad}$ in the range of $-20°$ to $20°$. The airspeed measurement shows an RMS error of $0.19\,\mathrm{m\,s^{-1}}$ with a peak-to-peak noise of $0.09\,\mathrm{m\,s^{-1}}$ and a range up to $28\,\mathrm{m\,s^{-1}}$. Therefore, the probe fulfills the requirements for the planned purpose of active turbulence suppression for fixed-wing UAV. Furthermore, the probe appears also suitable for a variety of other applications.**

I. INTRODUCTION

Unmanned Aerial Vehicles (UAV) often are equipped with airspeed sensors, however, are lacking directional information of the airflow like angle of attack (AOA) and sideslip angle (SSA). In this context, 3D printed probes [1] are promising to become low-cost and easily accessible alternatives to industrial measurement systems.

Investigations of simple measurement techniques, which also provide directional wind information, are of interest for UAV, as various application require these informations. On one hand applications known from manned aviation, such as flight envelope protection [2], flight control [3], as well as flight model identification and validation [4] are also of relevance for UAV. In this context, direct operational needs of UAV, such as stall protection [5], or also indirect needs for the development and validation of manned aircraft designs by means of unmanned model sized aircraft require directional airflow information. On the other hand applications which today are very rarely found in manned aviation may be of relevance for UAV.

Atmospheric research [6], e.g. to scan 3D wind fields with high spatial and temporal resolution, may expirience new possibilites by use of UAV swarms as safety concerns for operating multiple UAV in close proximity to each other are much smaller than for manned vehicles.

A very promising application, for which the probe in this paper is designed, is the suppression of turbulence effects in flight, which is particularly relevant for small UAV. Due to their low inertia and low flight altitudes they show to be highly susceptible to turbulence [7]. In contrast to gust load alleviation concepts which were implemented in manned aviation so far [8], more radical implementations of turbulence suppressing algorithms into the flight control of UAV can be conceivable, due to the lower certification requirements and faster development cycles.

For an aircraft flying in atmospheric turbulence, measuring related disturbance quantities such as airspeed, AOA, and SSA of the airflow are of particular interest for the effective suppression of disturbance effects on flight parameters, such as vertical acceleration, pitch moment, and roll moment. The disturbance measurements can be feedforwarded to the control surfaces of the aircraft to perform deflections, which reject the disturbance effects. Incorporating feedforward disturbance measurements is promising to drastically reduce turbulence effects in flight [9]. For this application very fast dynamics of the measurement principle are of particular interest, as time delays result in wrong phase correlations and in worst case intensify disturbance effects instead of suppressing them.

Common technologies for wind sensors include thermal anemometers [10], ultrasonic anemometers [11], wind LiDAR [12], wind vanes [13] and pressure measurements [14]. The expected

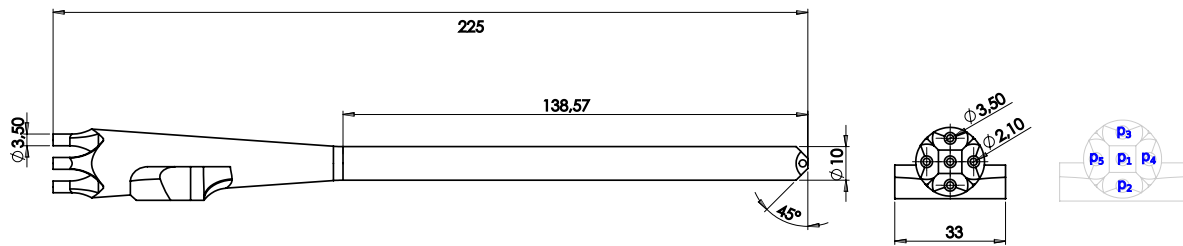[1] Corresponding author. galffy@acin.tuwien.ac.at

Fig. 1. Side view and front view of the 5-hole probe including its dimensions in mm. The positioning of the five pressure ports is denoted by the variables p_1, p_2, p_3, p_4, and p_5. The static port p_s is taken from inside the fuselage.

precision of thermal anemometry is to low for the envisaged task. Ultrasonic anemometers and wind LiDAR are assessed to be to complex for UAV integration. The bandwidth of wind vanes results to be to low for the requirements of turbulence suppression for UAV, as the mass of the vane first needs to be repositioned, which results in a low-pass characteristic. As a consequence, in this paper a 5-hole probe is designed, which in combination with high-bandwidth differential pressure sensors is expected to have very fast dynamic behavior. In this context, the contribution of this paper is a pressure sensor set-up, which only requires three pressure sensors, a simple wind tunnel calibration method, which makes use of the available UAV sensors to obtain reference angles, and the validation of the probe by actual atmospheric test flights by means of a fixed-wing UAV.

The design of the 3D printed probe as well as the integration into a fixed-wing UAV system are discussed in Section II. The most important aerodynamic relations are modelled in Section III. The probe is charaterized by means of a free jet wind tunnel in Section IV. Finally, a first test flight is performed in Section V, followed by a conclusion of the results and an outlook on related research topics.

II. PROBE DESIGN AND INTEGRATION

The high-dynamic measurement of wind quantities in flight to subsequently predict turbulence effects is the main interest for the design and implementation of the 5-hole probe in this paper.

The probe is installed at the nose of a fixed-wing UAS (Ranger 2400), which is tested to have a minimum airspeed of $8\,\mathrm{m\,s^{-1}}$ and a maximum airspeed of $28\,\mathrm{m\,s^{-1}}$. The aircraft is supposed to stay within a normal flight envelope, i.e. no aerobatic flight is performed. Therefore, a maximum range of AOA and SSA measurements of $-20°$ to $20°$ is required. For anticipating disturbance effects of atmospheric turbulence on the flight dynamics, the dynamic change of the airflow, but not the exact values of the stationary airflow are of interest. Therefore, offset errors due to misalignment of the probe mounting or misalignment of the flight controller, as well as the zero point accuracy of the underlying pressure sensors are not of primary interest, as long as the probe stays in its operational range. As the measurements shall be forwarded to the flight control surfaces to reduce disturbance effects, errors of the measured quantities reduce the achievable disturbance rejection. In this context, the application requires a maximum RMS error of $0.5\,\mathrm{m\,s^{-1}}$ for the airspeed and $2°$ for AOA and SSA in the given range. For the turbulence suppression task, the probe is required to measure frequencies up to $50\,\mathrm{Hz}$. Therefore, a minimum sampling rate of $100\,\mathrm{Hz}$ is required to comply with the Nyquist-Shannon sampling theorem. These requirements are summarized in Table I.

TABLE I

REQUIREMENTS FOR THE WIND SENSOR

Airspeed range	$8\,\mathrm{m\,s^{-1}}$ to $28\,\mathrm{m\,s^{-1}}$
AOA and SSA range	$-20°$ to $20°$
Airspeed error	$0.5\,\mathrm{m\,s^{-1}}$ RMS
AOA and SSA error	$2°$ RMS
Maximum offset error	maintain operational range
Minimum sampling rate	$100\,\mathrm{Hz}$

Figure 1 shows the side view and front view of the design of the 5-hole probe including its dimensions in mm. The 3D model and 3D printer

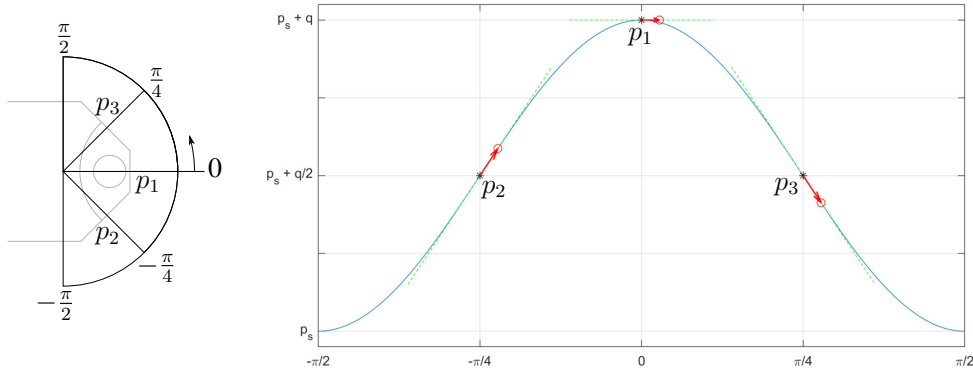Fig. 2. Expected surface pressure distribution at the probe tip as a function of the angle θ as indicated on the left scheme. The black stars denote the pressures p_1, p_2, and p_3 for $\alpha = 0$, i.e. symmetric airflow directly from the front. For a positive change of α the pressures shift to the right (red cycles) as indicated by the arrows.

settings are provided with this paper in a digital form. Figure 1 further show the positioning of the five pressure ports p_1, p_2, p_3, p_4, and p_5. The pressures are expected to be close to static pressure p_s with small deviations in the order of the dynamic pressure $q = \rho_0 \frac{V_a^2}{2}$. For the maximum airspeed $28\,\mathrm{m\,s^{-1}}$ and $\rho_0 = 1.225\,\mathrm{kg\,m^{-3}}$ a dynamic pressure $q_{max} = 480.2\,\mathrm{Pa}$ results, which is more than a factor of 200 smaller than the atmospheric pressure at sea level, which is in the order of $100\,\mathrm{kPa}$. Due to the small pressure differences compared to the absolute pressure values, three relative pressure sensors (SDP31) with high sensitivity are used instead of absolute pressure sensors. The range of the digital sensors is $-500\,\mathrm{Pa}$ to $500\,\mathrm{Pa}$ with a resolution of 16 bit, i.e., a least significant bit of $7.6\,\mathrm{mPa}$.

By connecting p_1, p_2, and p_4 to the positive pressure inputs and p_s, p_3, and p_5 to the corresponding negative inputs of the sensors, the measured differential pressure outputs result as

$$y_1 = p_1 - p_s \tag{1}$$
$$y_2 = p_2 - p_3 \tag{2}$$
$$y_3 = p_4 - p_5, \tag{3}$$

where the static port p_s is taken from the inside of the fuselage. The signals of the pressure sensors are connected via I2C to a Pixhawk 2.1 flight controller. The data logging is scheduled with 200Hz, thus, a factor 2 faster than required, c.f., Table I.

As the differential pressure sensors are sampling 10 times faster with 2kHz, they are configured to average the measurements between the data requests to further reduce the sensor noise. The flight controller among other quantities also logs the longitudinal acceleration a_x, the downwards positive vertical acceleration a_z, the pitch rate ω_y and the pilot's control inputs.

The expected aerodynamic characteristics of the probe, which are used to extract airflow information out of the pressure measurements, are discussed in the next section.

III. AERODYNAMIC MODELLING

The three differential pressure measurements y_1, y_2, and y_3, as introduced in Section II, are used to obtain information of the local air flow at the probe tip. In addition to the airspeed V_a, also directional information, i.e. the AOA α and SSA β, may be derived.

Figure 2 shows a scheme of the expected pressure distribution at the probe tip as a function of the indicated angle θ in the vertical plane for $\alpha = \beta = 0$, i.e. parallel airflow from the front. The $\cos(\theta)^2$-shape is based on the streamline projection method [15], which approximates the pressure distribution by projection of the free stream velocity on the local probe surface. For symmetry reasons an analogous distribution can be expected for the horizontal plane, which mainly depends on the SSA β, whereas the pressure distribution in the

vertical plane mainly depends on the AOA α. At the stagnation point, i.e. $\theta = 0$, the pressure port p_1 is expected to measure the sum of static pressure p_s and dynamic pressure $q = \rho_0 \frac{V_a^2}{2}$, where $\rho_0 = 1.225 \, \text{kg} \, \text{m}^{-3}$ denotes the air density of the international standard atmosphere at mean sea level, and V_a denotes the airspeed. Downstream of the probe tip, i.e. aft of $\theta = -\frac{\pi}{2}$ and $\theta = \frac{\pi}{2}$, the surface pressure is expected to decay back to static pressure p_s. The pressure ports p_2 and p_3 are located at $\theta = -\frac{\pi}{4}$ and $\theta = \frac{\pi}{4}$, where a high change of surface pressure in function of the AOA α is expected. As the differential pressure sensor measures $y_2 = p_2 - p_3$, the pressures p_2 and p_3 cancel out for $\alpha = 0$. Thus, determining the exact value of the offset, which is expected to be about $p_s + \frac{q}{2}$, is not possible with this set-up.

The main functionality of the probe becomes apparant, when the effect of an airflow change is considered in Figure 2. For positive AOA α the airflow approaches the probe tip from below. Therefore, pressure p_2 increases and p_3 decreases, as indicated by the red arrows mainly in a linear way. As p_1 is located at the stagnation point with maximum pressure, there is no first order dependency on α and β to be expected, i.e., $\frac{\partial p_1}{\partial \alpha} = \frac{\partial p_1}{\partial \beta} = 0$. Still, second order effects $\frac{\partial^2 p_1}{\partial \alpha^2}$ and $\frac{\partial^2 p_1}{\partial \beta^2}$ need to be corrected, which will be examined in wind tunnel tests in Section IV.

Based on the pressure distribution of Figure 2 and under the assumptions that the measurements of α in the vertical plane and β in the horizontal plane are sufficiently decoupled, a simple model with constant first order coefficients a_α and a_β and constant second order coefficients b_α and b_β, can be written as

$$p_1 = p_s + q_0 \tag{4}$$

$$p_2 = p_s + \frac{\alpha}{2a_\alpha} q \tag{5}$$

$$p_3 = p_s - \frac{\alpha}{2a_\alpha} q \tag{6}$$

$$p_4 = p_s + \frac{\beta}{2a_\beta} q \tag{7}$$

$$p_5 = p_s - \frac{\beta}{2a_\beta} q \tag{8}$$

with the uncorrected dynamic pressure

$$q_0 = y_1 = q - b_\alpha \alpha^2 q - b_\beta \beta^2 q. \tag{9}$$

For determining α and β independently from q, the coupled effects of wind direction and dynamic pressure, i.e. the terms αq and βq, need to be separated. To this end, the differential pressure measurements $y_2 = p_2 - p_3$ and $y_3 = p_4 - p_5$ are normalized by the measurement $y_1 = p_1 - p_s = q_0 \approx q$ to obtain the dimensionless coefficients

$$C_{\alpha,0} = \frac{y_2}{y_1} \approx \frac{p_2 - p_3}{q} = \frac{\alpha}{a_\alpha} \tag{10}$$

$$C_{\beta,0} = \frac{y_3}{y_1} \approx \frac{p_4 - p_5}{q} = \frac{\beta}{a_\beta}. \tag{11}$$

For higher values of α and β the quadratic terms $b_\alpha \alpha^2 q$ and $b_\beta \beta^2 q$ in (9) are expected to be too high to be neglected and will be corrected by means of wind tunnel calibration data in Section IV. The airflow quantities without correction, i.e., $V_{a,0}$, α_0, and β_0, can be calculated as

$$V_{a,0} = \sqrt{\frac{2q_0}{\rho_0}} \tag{12}$$

$$\alpha_0 = a_\alpha C_{\alpha,0} \tag{13}$$

$$\beta_0 = a_\beta C_{\beta,0}, \tag{14}$$

based on (9), (10), and (11) and serve as baseline to be compared with the corrected quantities. The parameters a_α and a_β reflect the characteristic of the probe to be able to retrieve directional airflow information and will be determined by wind tunnel calibration data.
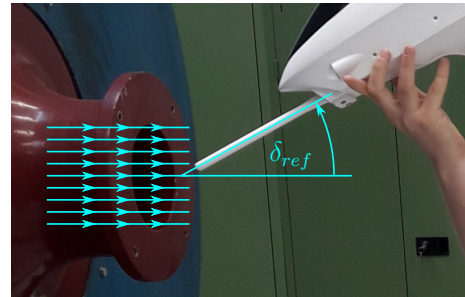
IV. WIND TUNNEL CALIBRATION

Fig. 3. Calibration of the 5-hole probe at the nozzle of an open jet wind tunnel. The probe is mounted on the UAV body, which is manually tilted while the probe tip stays in the middle of the airstream. The reference angle δ_{ref} is determined by gravitational acceleration measurements of the internal accelerometers of the UAV and used for calibration references α_{ref} and β_{ref}.

The objective of the wind tunnel calibration is to identify the parameters a_α and a_β, and to compensate for the quadratic dependence (9) to obtain improved measurement results of α, β, and V_a. For calibrating the probe an open jet wind tunnel with a circular nozzle with a diameter of $120\,\mathrm{mm}$ is used. To check whether the obtained wind information is valid for various airspeeds, measurements are conducted for three different reference airspeeds $V_{a,ref}$ of $17.2\,\mathrm{m\,s^{-1}}$, $21.9\,\mathrm{m\,s^{-1}}$, and $26.4\,\mathrm{m\,s^{-1}}$. For the wind tunnel testing the probe is already mounted on the aircraft body as described in Section II, but without wings to avoid vibrations. As the microcontroller is logging the pitch angle of the aircraft, this information may be used to determine the reference angle δ_{ref} of the airflow, as indicated in 3. For SSA measurements the aircraft is rotated by $90°$ around the roll axis. Thereby, also for SSA measurements the pitch angle can be used as reference angle, instead of the yaw angle. This is preferred, as varying the pitch angle also changes the longitudinal acceleration measurement a_x and thus allows to have a second reference information based on the orientation of the gravitational acceleration with the relation $a_x = 9.81\,\mathrm{m\,s^{-2}}\sin(\delta_{ref})$, i.e., $a_x = 0\,\mathrm{m\,s^{-2}}$, when the aircraft is straight and level, and $a_x = 9.81\,\mathrm{m\,s^{-2}}$, when the aircraft's nose points down. As the accelerometer measurements a_x show to be the most accurate reference data, the reference airflow angles are determined as

$$\delta_{ref} = \arcsin\left(\frac{a_x}{9.81\,\mathrm{m\,s^{-2}}}\right), \qquad (15)$$

with $\alpha_{ref} = -\delta_{ref}$ for a roll angle of $0°$, i.e. wings level, and $\beta_{ref} = \delta_{ref}$ for a roll angle of $90°$, i.e. the right wing pointing down.

First, the dependence of the measured dynamic pressure q_0 and thus the derived airspeed

$$V_{a,0} = \sqrt{\frac{2q_0}{\rho_0}} \qquad (16)$$

as a function of α and β is examined. To this end α is manually varied for various angles of β, which are manually kept approximately constant. Thereafter, the aircraft is rotated by $90°$ around the roll axis, and then in the same way β is varied for approximately constant values of α. With $C_{\alpha,0}$ and $C_{\beta,0}$ according to (10) and (11) the resulting
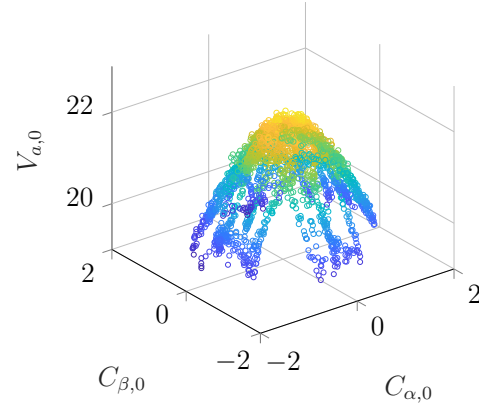

Fig. 4. Mapping of $V_{a,0}$ as a function of $C_{\alpha,0}$ and $C_{\beta,0}$ for constant $V_{a,ref} = 21.9\,\mathrm{m\,s^{-1}}$. The quadratic dependence on α and β results in a paraboloid shape instead of a desired flat plane with $21.9\,\mathrm{m\,s^{-1}}$.

mapping $V_{a,0}(C_{\alpha,0}, C_{\beta,0})$ is shown in Figure 4. As expected from the pressure distribution around p_1 in Figure 2, a quadratic dependence on α and β, can be observed resulting in a paraboloid shape according to (9).

The reference airspeed $V_{a,ref} = V_{a,0}(0,0) = 21.9\,\mathrm{m\,s^{-1}}$ is kept constant during variation of α and β, thus, also the airspeed output V_a shall be corrected to be constant. To compensate for the quadratic dependence, correction terms with constant parameters γ_α and γ_β are chosen according to

$$V_a = V_{a,0}(1 + \gamma_\alpha C_{\alpha,0}^2 + \gamma_\beta C_{\beta,0}^2). \qquad (17)$$

To minimize the error $V_{a,ref} - V_a$ the least squares optimization problem

$$\min_{\mathbf{p}}(\mathbf{y} - \mathbf{Sp})^{\mathrm{T}}(\mathbf{y} - \mathbf{Sp}) \qquad (18)$$

with

$$\mathbf{y} = \mathbf{V}_{a,ref} - \mathbf{V}_{a,0} \qquad (19)$$

$$\mathbf{S} = \begin{bmatrix} \mathbf{V}_{a,0} \circ \mathbf{C}_{\alpha,0}^{\circ 2} & \mathbf{V}_{a,0} \circ \mathbf{C}_{\beta,0}^{\circ 2} \end{bmatrix} \qquad (20)$$

$$\mathbf{p} = \begin{bmatrix} \gamma_\alpha & \gamma_\beta \end{bmatrix}^{\mathrm{T}} \qquad (21)$$

is solved, where $\circ$ denotes the element wise operation and $\mathbf{V}_{a,ref}$, $\mathbf{V}_{a,0}$, $\mathbf{C}_{\alpha,0}$, and $\mathbf{C}_{\beta,0}$ are vectors containing the N=88198 measurement points. The obtained parameters $\gamma_\alpha = 0.0570$ and $\gamma_\beta = 0.0569$ are almost identical, what was expected due to symmetrical reasons.
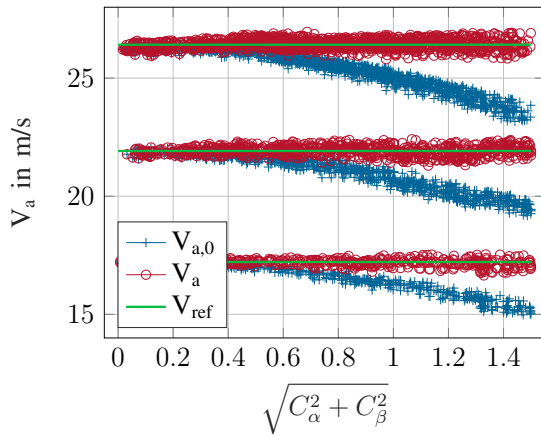
Fig. 5. Comparison of $V_{a,0}$, V_a and $V_{a,ref}$ as a function of $\sqrt{C_\alpha^2 + C_\beta^2}$ for the three test speeds $17.2\,\mathrm{m\,s^{-1}}$, $21.9\,\mathrm{m\,s^{-1}}$, and $26.4\,\mathrm{m\,s^{-1}}$. The correction of the quadratic dependences of $V_{a,0}$ on C_α and C_β reduces the error between the airspeed output V_a and the respective reference speed $V_{a,ref}$.

For validation of the effectiveness of the correction, Figure 5 shows $V_{a,0}$, V_a and $V_{a,ref}$ for the three test speeds as a function of $\sqrt{C_{\alpha,0}^2 + C_{\beta,0}^2}$, i.e., the distance from the origin in Figure 4. Thereby, the quadratic dependences of $V_{a,0}$ on C_α and C_β becomes very clear. The corrected airspeed V_a indeed shows much less error to the respective reference speed $V_{a,ref}$, resulting in a reduction of the overall RMS error of the airspeed measurement from $1.21\,\mathrm{m\,s^{-1}}$ to $0.187\,\mathrm{m\,s^{-1}}$. It is important to mention, that for the calibration (17) only the differential pressure measurements y_1, y_2, y_3, and an airspeed reference $V_{a,ref}$ are necessary, but no reference angle information is needed, c.f. (10) and (11).

For the calibration of AOA α and SSA β the corresponding reference angle is determined according to (15). The procedure is the same for both angles and will be shown for AOA α. The fundamental relation for determining α from the differential pressure measurement y_2 is

$$\frac{y_2}{q} = \frac{p_3 - p_1}{q} = \frac{\alpha}{a_\alpha}. \tag{22}$$

As $C_{\alpha,0}$ is normalized by $y_1 = q_0$ instead of q a distortion can be expected. Therefore, the correction term (17) for $V_{a,0}$ can be used according

to the relation

$$q = \frac{\rho_0}{2}V_a^2 = \frac{\rho_0}{2}V_{a,0}^2(1 + \gamma_\alpha C_{\alpha,0}^2 + \gamma_\beta C_{\beta,0}^2)^2 =$$
$$q_0(1 + \gamma_\alpha C_{\alpha,0}^2 + \gamma_\beta C_{\beta,0}^2)^2 \tag{23}$$

to obtain the corrected coefficent

$$C_\alpha = \frac{y_2}{q} = \frac{y_2}{q_0(1 + \gamma_\alpha C_{\alpha,0}^2 + \gamma_\beta C_{\beta,0}^2)^2} =$$
$$\frac{C_{\alpha,0}}{(1 + \gamma_\alpha C_{\alpha,0}^2 + \gamma_\beta C_{\beta,0}^2)^2}. \tag{24}$$
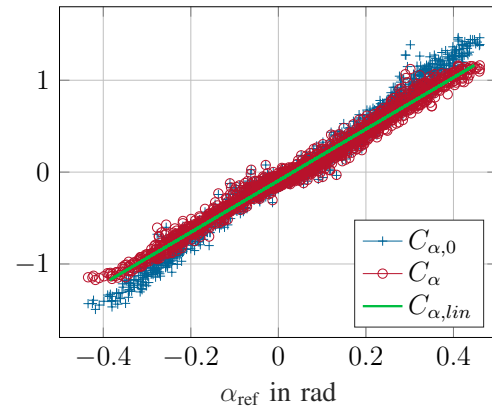
In Figure 6 the coefficients $C_{\alpha,0}$ and C_α are

Fig. 6. Comparison of the coefficients $C_{\alpha,0}$ and C_α, which is calculated with the correction (24), as a function of α_{ref}. $C_{\alpha,lin}$ shows the linear approximation of C_α.

plotted as a function of α_{ref}. With the correction (24) the linearity of C_α improves, especially for $|\alpha_{ref}| > 0.2$, where $C_{\alpha,0}$ already shows significant distortions due to being normalized by q_0 instead of q. $C_{\alpha,lin}$ shows the linear approximation of C_α. To this end, a least squares problem is solved with N=53871 measurement points to obtain optimal parameters $a_{0,\alpha} = 0.0334\,\mathrm{rad}$ and $a_{1,\alpha} = 0.3563\,\mathrm{rad}$ according to

$$\alpha_{ref} = a_{0,\alpha} + a_{1,\alpha}C_\alpha. \tag{25}$$

In the same way $a_{0,\beta} = 0.0152$ and $a_{1,\beta} = 0.3556$ can be determined for the SSA β with N=34327 measurement points. The value of $a_{1,\alpha}$ and $a_{1,\beta}$ are almost identical due to reasons of symmetry. The offsets $a_{0,\alpha}$ and $a_{0,\beta}$ arise due to misalignment of the probe and the autopilot system. If needed, the offset may be reduced by more accurate alignment of the probe. Finally, with the parameters $a_{0,\alpha}$ and
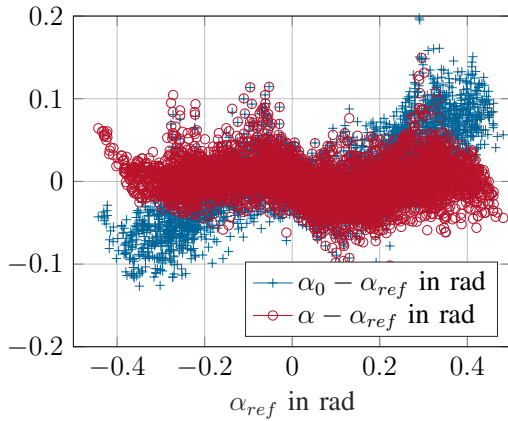
Fig. 7. Comparison of the error $\alpha_0 - \alpha_{ref}$ and the error $\alpha - \alpha_{ref}$, which is calculated with the correction (24).

$a_{1,\alpha}$ the AOA α can be calculated for given C_α analogously to (25) by $\alpha = a_{0,\alpha} + a_{1,\alpha}C_\alpha$. Figure 7 shows the error $\alpha - \alpha_{ref}$ and compares it to the error $\alpha_0 - \alpha_{ref}$ of α_0, which is calculated without correction (24). The correction reduces the RMS from $0.0407\,\text{rad}$ to $0.0242\,\text{rad}$, which complies with the requirement of Table I.

As a first summary the probe of Section II with the calibration of this Section fulfills the requirements of Table I. Figure 8 illustrates the Wind tunnel calibration maneuvers for the three different reference airspeeds $V_{a,ref}$. For each speed the reference AOA α_{ref} is manually varied between approximately $-0.4\,\text{rad}$ and $0.4\,\text{rad}$. For $|\alpha_{ref}| > 0.2$ the uncorrected quantities α_0 and $V_{a,0}$ show significant deviations, while the corrected quantities α and V_a show only small errors.

V. TEST FLIGHT

As the requirements are satisfied in wind tunnel tests, a first flight test is being performed to validate the performance of the probe in the actual test environment. The probe is integrated into the UAV system as stated in Section II. To analyze the behavior of the probe and aircraft without external disturbance inputs such as turbulence, very calm weather conditions are pursued, which are found at sun rise during high-pressure weather conditions. An open loop identification maneuver is flown by means of a frequency sweep elevator signal, which is superposed to the manual control of the test

pilot. The pilot itends to give only low frequent control inputs to maintain the equilibrium state of leveled flight without interfering the identification signal. The time evolution of the measured quantities α, V_a, $-a_z$, ω_y during the maneuver are depicted in 9. The first $6\,\text{s}$ the aircraft flies as autonomous system without any control input. Only small variations of the quantities can be observed, consisting of a remaining low-frequent phugoid oscillation and the high-frequent noise of the sensors. The phugoid oscillation, which is a lightly damped exchange of kinetic and potential energy, becomes apparent as the airspeed V_a varies between $11\,\text{m s}^{-1}$ and $13\,\text{m s}^{-1}$ with an oscillation period of about $T_{ph} \approx 6\,\text{s}$. This is in accordance with the expected flight dynamics $T_{ph,0} = 5.5\,\text{s} = 0.453V_a$, c.f., [16]. The peak-to-peak noise is $0.09\,\text{m s}^{-1}$ for V_a, and $3\,\text{mrad}$ for α and β.

At $t = 6\,\text{s}$ the elevator frequency sweep starts to excite the aircraft for a duration of $20\,\text{s}$ starting at $3\,\text{Hz}$ and decreasing linearly with time t to $0.3\,\text{Hz}$. Exciting higher frequencies first is chosen to delay the excitation of the phugoid mode which causes an alteration of the airspeed. In this context, the eigenfrequency of $f_{ph} = \frac{1}{T_{ph}} \approx 0.17\,\text{Hz}$ is already close to $0.3\,\text{Hz}$. In consequence, the airspeed variation isn't noticeable for higher frequencies, which are excited at the beginning of the maneuver, but increase rapidly for $t > 20\,\text{s}$.

The vertical acceleration $-a_z$, which is mainly generated by the lift of the wings, is about $9.81\,\text{m s}^{-2}$ in the equilibrium state of straight and level flight to compensate the gravitational acceleration. This initial value is superposed by an amplitude of up to $15\,\text{m s}^{-2}$ caused by the elevator excitation signal. It can be noted that the vertical acceleration $-a_z$ strongly relates to the variation of the AOA α. The short-period mode results in a second order low-pass behavior of α and $-a_z$, which can clearly be observed, as the amplitude increases with lower frequencies.

The pitch rate ω_y shows an amplitude of $1\,\text{rad s}^{-1}$. As the probe tip is positioned at a distance $d_{CG} = 0.5\,\text{m}$ in front of the center of gravity, c.f., Figure 3, ω_y causes a perpendicular change of the local airflow at the probe tip by
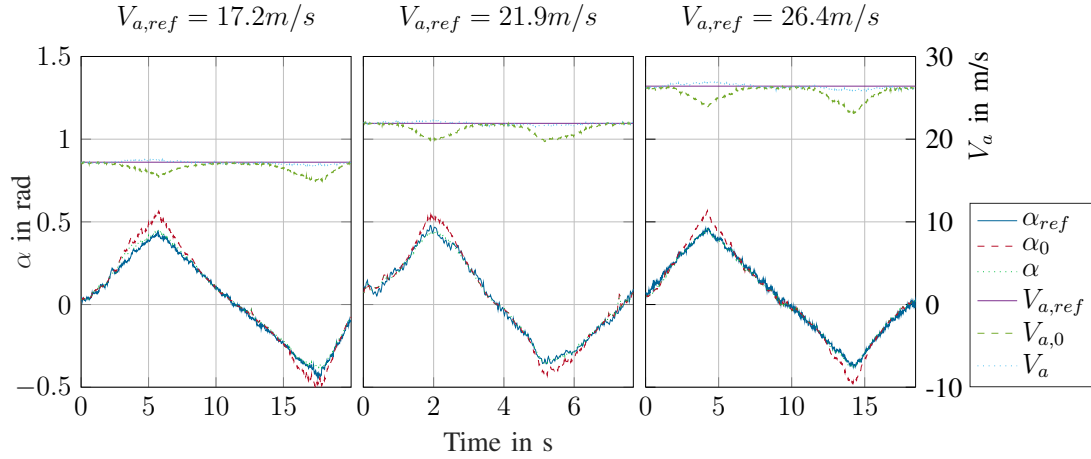
Fig. 8. Wind tunnel calibration maneuvers for $V_{a,ref}$ of $17.2\,\mathrm{m\,s^{-1}}$, $21.9\,\mathrm{m\,s^{-1}}$, and $26.4\,\mathrm{m\,s^{-1}}$. For each speed the reference AOA α_{ref} is manually varied between approximately $-0.4\,\mathrm{rad}$ and $0.4\,\mathrm{rad}$. For $|\alpha_{ref}| > 0.2$ the uncorrected quantities α_0 and $V_{a,0}$ show significant deviations, while the corrected quantities α and V_a show only small errors.
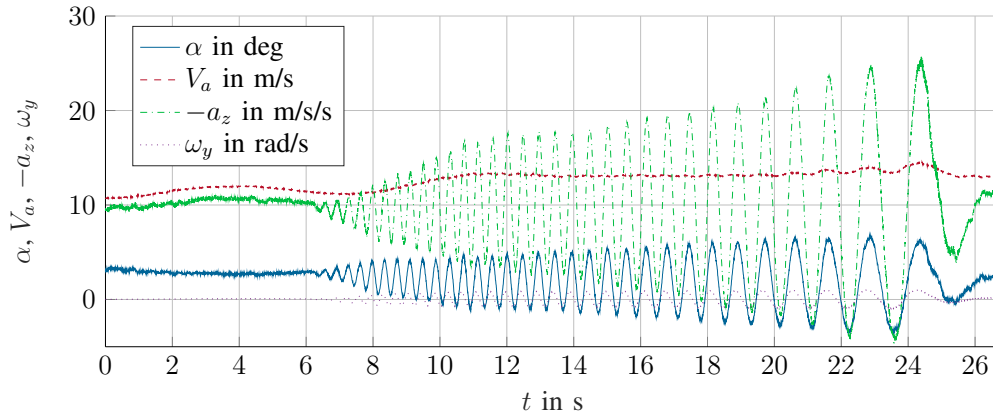

Fig. 9. Measured flight parameters α, V_a, $-a_z$, ω_y for an identification maneuver in the frequency range of the short-period mode. The first $6\,\mathrm{s}$ the aircraft flies as autonomous system without any control input. Starting at $t = 6\,\mathrm{s}$ the aircraft is excited by the elevator with a frequency sweep from $3\,\mathrm{Hz}$ to $0.3\,\mathrm{Hz}$.

$V_{a,\perp} = d_{CG}\omega_y$. Therefore, a correction

$$\alpha_{CG} = \alpha + \frac{d_{CG}\omega_y}{V_a} \qquad (26)$$

can be calculated to obtain the AOA α_{CG}, which would be observed at the center of gravity.

With the correction (26) a final evaluation of the acccuracy of the probe can be carried out. As the identificaion maneuver is performed with wings leveled and in very calm air, the angle of attack at the center of gravity α_{CG} results as the difference of the pitch angle θ and the flight path angle γ,

[16]. Thus, with the relations $\dot{\theta} = \omega_y$ and $\dot{\gamma} = \frac{-a_z}{V_a}$ an in-flight reference of the derivative $\dot{\alpha}_{CG,ref}$ can be determined as

$$\dot{\alpha}_{CG,ref} = \dot{\theta} - \dot{\gamma} = \omega_y + \frac{a_z}{V_a}, \qquad (27)$$

which can directly be calculated by the quantities depicted in Figure 9. This reference can be compared to $\dot{\alpha}_{CG}$, which results from the direct α measurement of the probe after correction (26) and numerical differentiation. Figure 10 shows $\dot{\alpha}_{CG,ref}$, $\dot{\alpha}_{CG}$ and $\dot{\alpha}$, which is the direct numerical differentiation of α without correction (26). A
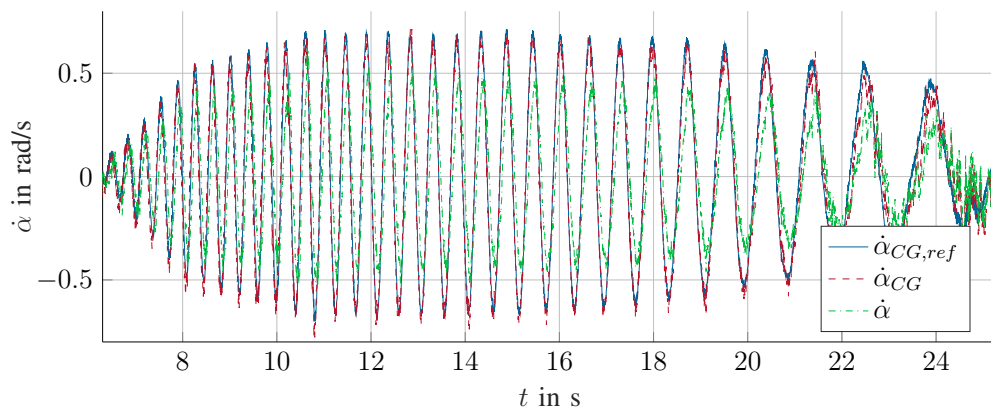
Fig. 10. Comparison of reference AOA at the center of gravity $\dot{\alpha}_{CG,ref}$, which is calculated using the relation (27), with the AOA measurement $\dot{\alpha}_{CG}$ including the correction (26) and the uncorrected AOA measurement $\dot{\alpha}$.

very good compliance of $\dot{\alpha}_{CG,ref}$ and $\dot{\alpha}_{CG}$ can be observed, whereas $\dot{\alpha}$ shows significant deviations due to the local change of the airflow $V_{a,\perp} = d_{CG}\omega_y$.

Summarizing, the probe shows very good performance in flight with low noise, reflecting expected flight dynamics of the aircraft, and consistency to alternative reference quantities. The proposed wind tunnel calibration method by means of internal measurements of the UAV reduces the calibration effort and proved to be suitable to determine the probe parameters with sufficient accuracy. Altogether, 3D printed 5-hole probes in combination with high-bandwidth differential pressure sensors are assessed capable to provide easy access to directional airflow information for UAV saving costs and development time.

VI. CONCLUSION AND OUTLOOK

In this paper a 3D printed 5-hole probe is calibrated by means of wind tunnel test data and validated by means of atmospheric test flights with the objective to facilitate high-dynamic wind measurements for UAV including directional airflow information. In conclusion the probe fulfills the requirements given by the intended application of active turbulence suppression.

The airspeed measurement results to have a range up to $28\,\mathrm{m\,s^{-1}}$ and a RMS error of $0.19\,\mathrm{m\,s^{-1}}$ with a peak-to-peak noise of $0.09\,\mathrm{m\,s^{-1}}$. The measurements of AOA and SSA in the range of $-20°$ to $20°$ result to have a RMS error of

$24\,\mathrm{mrad}$ with a peak-to-peak noise of $3\,\mathrm{mrad}$. The sampling rate of $200\,\mathrm{Hz}$ in principle allows to measure wind changes up to $100\,\mathrm{Hz}$. To analyze the dynamical limits of the measurement principle further investigations with known rapid changes of the airflow, e.g., a turbulence generator, would be necessary.

The quadratic error of the airspeed measurement at the tip of the probe due to the shifting stagnation point is corrected by quadratic terms reducing the RMS error from $1.21\,\mathrm{m\,s^{-1}}$ to $0.187\,\mathrm{m\,s^{-1}}$. The calibration is performed by means of a free jet wind tunnel. Furthermore, a correction term is introduced to account for the position of the probe in front of the aircraft instead of the center of gravity. This reduces errors, which are generated by angular rates, due to local perpendicular airflows at the probe tip. The performance of the probe in-flight is validated by a first test flight with a dynamic frequency sweep maneuver.

In summary, the probe is fairly simple to produce and fulfills the requirement for the envisaged task of active turbulence suppression. To this end, in future work the measured quantities V_a, α, and β will be feedforwarded to the flight control surfaces to reject disturbance effects. Further investigations to compare the probe with other wind sensing technologies, e.g., Wind LiDAR, are promising to identify advantages and disadvantages of fast differential pressure sensors for high-dynamic wind measurements.

ACIN

REFERENCES

[1] B. F. Hall and T. Povey, "The Oxford Probe : an open access five-hole probe for aerodynamic measurements," *Measurement Science and Technology*, vol. 28, p. 035004, 2017.

[2] W. Falkena, C. Borst, Q. P. Chu, and J. A. Mulder, "Investigation of practical flight envelope protection systems for small aircraft," *Journal of Guidance, Control, and Dynamics*, vol. 34, no. 4, pp. 976–988, 2011.

[3] S. H. Lane and R. F. Stengel, "Flight control design using non-linear inverse dynamics," *Automatica*, vol. 24, no. 4, pp. 471–483, 1988.

[4] M. B. Tischler and R. K. Remple, *Aircraft and Rotorcraft System Identification*. AIAA education series, 2006.

[5] I. Yavrucuk, S. Unnikrishnan, and J. V. R. Prasad, "Envelope protection for autonomous unmanned aerial vehicles," *Journal of Guidance, Control, and Dynamics*, vol. 32, no. 1, pp. 248–261, 2009.

[6] S. Martin, J. Bange, and F. Beyrich, "Meteorological profiling of the lower troposphere using the research UAV "M2AV Carolo"," *Atmospheric Measurement Techniques*, vol. 4, no. 4, pp. 705–716, 2011.

[7] J. Smith, J. Su, C. Liu, and W. H. Chen, "Disturbance Observer Based Control with Anti-Windup Applied to a Small Fixed Wing UAV for Disturbance Rejection," *Journal of Intelligent and Robotic Systems: Theory and Applications*, vol. 88, no. 2-4, pp. 329–346, 2017.

[8] A. Wildschek, R. Maier, M. Hromcik, T. Hanis, A. Schirrer, M. Kozek, C. Westermayer, and M. Hemedi, "Hybrid controller for gust load alleviation and ride comfort improvement using direct lift control flaps," *Proceedings of Third European Conference for Aerospace Sciences*, vol. 3, no. 6, pp. 101–102, 2008.

[9] N. Fezans, H.-D. Joos, and C. Deiler, "Gust load alleviation for a long-range aircraft with and without anticipation," *CEAS Aeronautical Journal*, pp. 1–25, 2019.

[10] M. Ashauer, H. Glosch, F. Hedrich, N. Hey, H. Sandmaier, and W. Lang, "Thermal flow sensor for liquids and gases," *American Society of Mechanical Engineers, Dynamic Systems and Control Division (Publication) DSC*, vol. 66, pp. 427–432, 1998.

[11] T. Nakai and K. Shimoyama, "Ultrasonic anemometer angle of attack errors under turbulent conditions," *Agricultural and Forest Meteorology*, vol. 162, pp. 14–26, 2012. [Online]. Available: http://dx.doi.org/10.1016/j.agrformet.2012.04.004

[12] N. Schmitt, W. Rehm, T. Pistner, H. Diehl, P. Nave, and G. Jenaro Rabadan, "A340 flight test results of a direct detection onboard UV LIDAR in forward-looking turbulence measurement configuration," *15th Coherent Laser Radar Conference CLRC*, no. June, pp. 22–26, 2009.

[13] J. Wieringa, "Evaluation and Design of Wind Vanes," *Journal of Applied Meteorology*, vol. 6, no. 6, pp. 1114–1122, 1967.

[14] R. G. Dominy and H. P. Hodson, "An investigation of factors influencing the calibration of 5-hole probes for 3-D flow measurements," *ASME 1992 International Gas Turbine and Aeroengine Congress and Exposition, GT 1992*, vol. 1, 1992.

[15] R. Willinger, "A three-hole pressure probe exposed to wall proximity effects: experimental, numerical and analytical investigation," *Conference on Modelling Fluid Flow, Budapest 2006*.

[16] R. F. Stengel, *Flight dynamics*. Princeton University Press, 2004.